# Garnet fracturing reveals ancient unstable slip events hosted in plate interface metasediments

Samuel Angiboust[1*]

Paraskevi Io Ioannidi[2]

Iskander Muldashev[3,4]

[1] ENS de Lyon, LGL-TPE, CNRS, 46 Allée d'Italie, Lyon, France

[2] Department of Earth Sciences, Vrije Universiteit Amsterdam, Amsterdam, The Netherlands

[3] GFZ German Research Centre for Geosciences, Potsdam, Germany

[4] TU Bergakademie Freiberg, Freiberg, Germany

*: *corresponding author*: S. Angiboust, samuel.angiboust@ens-lyon.fr

**This is a non-peer reviewed preprint that has been submitted to Earth and Planetary Science Letters (EPSL).**

## ABSTRACT

A paradox exists between the great number of intermediate-depth earthquakes occurring along active subduction interfaces worldwide and the extreme scarcity of paleo-seismic events recorded in exhumed metasedimentary rocks from ancient subduction zones. Recrystallization, shearing as well as exhumation-related overprinting generally contribute to the nearly-complete erasing of markers of unstable slip events in metamorphic rocks. We herein focus on a sample from an ancient deep thrust from a Cretaceous High-Pressure paleo-accretionary complex in Chilean Patagonia. A representative, moderately foliated micaschist exhibits broken garnet crystals that host a dense network of healed micro-fractures. While garnet fragments appear thoroughly disaggregated along the main foliation, the matrix that has completely recrystallized hardly records brittle deformation. We employ a 2D visco-elasto-plastic numerical modelling approach in order to investigate the mechanical conditions that enable the fracturing of isolated garnet grains in a relatively weak matrix. The rupture of these stiff grains is achieved in our models at strain rates faster than $10^{-10}$ /s to $10^{-12}$ /s for elevated pore fluid pressures (80 to 99% of the lithostatic value, respectively). Since high pore fluid pressures prevail in deep subduction interface settings, it is suggested that the rupture of these garnet crystals occurred through cataclastic deformation via (transient) slip rate acceleration, perhaps as a consequence of localized slip associated with slow to normal earthquakes. Upon slip rate deceleration, viscous disaggregation of the broken garnet clasts occurred along with the erasing of the matrix cataclastic fabric.

*Keywords*: numerical modelling, garnet, fracturing, metasediment, paleoseismicity

## 1. INTRODUCTION

Thousands of earthquakes occur every year at the base of the seismogenic zone along the ‘upper seismic plane’ in active subduction margins worldwide at conditions where the downgoing crust experiences metamorphic recrystallization under blueschist to eclogite-facies conditions (most commonly between 35 and 70 km depth and 300-600°C depending on the geothermal gradient; Hacker et al., 2003). Geodetic data has also demonstrated that this region of the plate interface hosts abundant slow earthquakes and post-seismic slip of megathrust ruptures (e.g. Alaska: Freymuller et al., 2008; Chile: Lange et al., 2012; Luo & Wang, 2021). The physical nature of the processes that cause the upper-plane seismicity remains a matter of debate (e.g. Shiina et al., 2013; Incel et al., 2017). High-resolution seismological studies confirm that the bulk of this upper plane seismicity is hosted in the downgoing crust (e.g. Sippl et al., 2018) even though the resolution does not enable distinguishing whether these earthquakes nucleate in metasediments or in the underlying mafic crust.

Exhumed metamorphic rocks represent precious witnesses of deformation processes taking place at depth along the subduction interface (e.g. Bebout & Penniston-Dorland, 2016; Behr & Bürgmann, 2021). On the one hand, recent field and structural investigations have emphasized the prevalence of pressure-solution processes during creep in both hydrothermalized metabasalts and metasediments which together contribute to maintaining the plate interface strength at relatively low stress levels on geological timescales (e.g. Wassman & Stöckhert, 2013a; Tulley et al., 2020; Condit et al., 2022). On the other hand, the scarce evidence for paleoseismicity in exhumed subduction zone high-pressure (HP) metamorphic rocks appears to be restricted to relatively stiff lithologies like metagabbros in the form of fault-zone rocks such as 'pseudotachylytes' (John & Schenk, 2006; Austrheim & Andersen, 2004) or 'eclogite breccias' (Angiboust et al., 2012) as well as within 'foliated cataclasites' in blueschist-facies metabasalts (Muñoz-Montecinos et al., 2021).

To our knowledge, no evidence for fast-slip brittle structures (i.e. structures on which slip occurred at the order of millimeters to meters per second) has been identified in deep-seated (T>450°) metasedimentary rocks from ancient subduction interface settings. This observation can easily be explained by (i) the relatively weak nature of quartz, carbonate and mica-bearing lithologies that dominantly compose the matrix of HP metasedimentary rocks (e.g. Behr et al., 2022; Smye & England, 2023 and references therein) (ii) the long residence time of accreted metasediments in deep duplex structures forming above the plate interface that enable petrological re-equilibration and the destruction of previously-formed brittle fabrics (e.g. Sibson, 1980; Kirkpatrick & Rowe, 2013) and (iii) the high pore fluid pressures that also catalyze re-equilibration and recrystallization processes along grain boundaries.

This paradox calls for a re-investigation of microstructures in exhumed HP metasediments, in particular within 'strong' minerals which may have greater chances to preserve remnants of 'lost' unstable slip events in their inner structure. We herein focus on the aspect, the size distribution and the chemical zoning patterns of broken garnet crystals in a micaschist sample from the Cretaceous Patagonian HP paleo-accretionary belt. Because stiff, isolated crystals such as garnet are expected to rotate –instead of breaking– during the shearing of a rheologically weak metasedimentary matrix (e.g. Passchier et al., 1992), we perform numerical modelling investigations in order to identify the physical parameters that can allow the fracturing of a strong particle in a relatively low viscosity environment.

## 2. GEOLOGICAL SETTING

The Diego de Almagro island represents one of the very rare exposures of the Mesozoic Chilean paleo-accretionary complex (Hervé & Fanning, 2003; Willner et al., 2004) and the first occurrence of eclogite-facies metamorphism in Chile (Hyppolito et al., 2016). The three main units exposed on this island have been formed by episodic basal accretion of material derived from the Pacific oceanic plate during Jurassic to Cretaceous times (Fig.1a; Angiboust et al., 2018). The studied sample (#47a) has been collected in the uppermost part of the 'garnet amphibolite' unit in the footwall of the Puerto Shear Zone, a major tectonic contact interpreted as an ancient subduction interface after accretion of the overlying Lazaro unit during the middle Jurassic (Fig.1b; Angiboust et al., 2018). Petrological investigations, thermodynamic modeling and ion probe U-Pb zircon rim dating have shown that peak burial conditions were reached at around 130 Ma, for a pressure (P) of c.1.7 GPa and a temperature (T) of 550-570°C (Hyppolito et al., 2016; Angiboust et al., 2018). The garnet amphibolite unit (in green in figure 1b) has been re-equilibrated upon exhumation along the subduction interface at 1.3 GPa (approximately 45 km depth; Fig.1c), where it underwent fracturing and shearing associated with moderate amphibolitization (Hyppolito et al., 2016). Then, it has been juxtaposed to the existing duplex and got later exhumed via long-lived underplating processes throughout the entire fore-arc crust (e.g. Angiboust et al., 2022).

## 3. PETROGRAPHIC OBSERVATIONS

The matrix of the micaschist #47a (Fig.2a,b) is composed of quartz (~30 vol.%), white mica (phengite, ~15 %), Na-Ca amphibole (~15 %), garnet (~12 %), albite (~12 %), epidote (~6 %), diopside (~5 %), chlorite (~3 %) and rutile-titanite (2 %). Rare crystals of omphacite, glaucophane and chloritoid, remnants from the eclogite-facies stage, are locally preserved as inclusions in garnet mantles (Hyppolito et al., 2016). The moderately strained matrix has recrystallized during an upper amphibolite-facies shearing event associated with exhumation at c.120 Ma (multi-mineral Rb-Sr dating; Hyppolito et al., 2016, 2019; Fig.1c). This event led to the partial re-equilibration of peak pressure garnet (garnet I) along its rims (garnet II). These two garnet generations, optically distinguishable on figure 2a, can be identified on back-scattered electron mode at the scanning electron microscope (SEM; Fig.2e; see Appendix for analytical conditions and for additional textural images). Automated surface estimations indicate that garnet I represents 10 surf. % and garnet II 2 surf. % of the area mapped in figure 2e. Garnet internal structure exhibits a general increase of its XMg content towards the rims (Fig.2c).

Numerous chemical oscillations, well-marked on the Mn map (Fig.2d), are transected by several overgrowths (white arrow) and crosscut by numerous healed micro-fractures observed within both garnet generations (Fig.2g,h). These micro-fractures are well expressed on the XMg map and connect the matrix with the garnet interior. Angular, broken garnet I clasts are commonly rimmed by a euhedral, facetted garnet II generation, that may or may not exhibit fracturing (Fig.2h,i; see also Appendix). Most large garnet crystals display healed fractures cutting straight across the crystal nearly linearly (Fig.2e,g; Appendix). In addition to micro-fracturing, some of the garnet zoning patterns display indentation features (see white arrows on Figs.2d,f) and subsequent enhanced garnet facet dissolution (e.g. Wassman & Stöckhert, 2013b). No clear evidence for subcritical crack growth (in the sense of Atkinson, 1984) has been detected using BSE or X-ray imaging. Garnet clast diameter typically ranges from several tens of microns to c.4 mm. Most of the garnet I clasts exhibit a surface smaller than 0.05 mm² (Appendix).

The matrix around garnet crystals exhibits only very discrete evidence for fracturing: microstructural evidence of fracturing has been only detected in albite porphyroclasts using optical cathodoluminescence imaging (see Appendix). The vast majority of the crystals forming the matrix exhibit a moderate shape-preferred orientation (especially white micas) along with indication of crystal-plastic deformation (well visible in quartz) as well as extensive evidence for pressure solution creep processes (PSC; see also Muñoz-Montecinos et al., 2020 for similar observations in Chilean basement rocks). Last, we note that similar (but less well-visible) fracturing patterns were observed in garnet from other samples from the same unit (the garnet amphibolite unit, Fig.1b; see Appendix), indicating the pervasiveness nature of the studied fracturing process along the Puerto Shear Zone.

# 4. NUMERICAL MODELING

## 4.1 Modeling approach

In order to model simple shear of a matrix with garnet inclusions we use the thermomechanical Finite Element Method (FEM) code SLIM3D (Popov & Sobolev, 2008), which solves the conservation equations of mass, momentum, and energy. The code uses a marker-in-cell method and employs a visco-elasto-plastic deformation pattern. The finite elements are isometric with a size of 0.1 mm while the 2D model domain is 105 mm wide and 50 mm deep (Figure 3). The garnet crystals of fixed size (diameter equals 5mm) are distributed randomly covering 10% of the model area. To create homogeneous distribution and prevent boundary effects, garnet crystals are distributed with the rule that none of them can be positioned at the distance smaller than the garnet diameter from other garnet or model boundary.

We use temperature of 550 ºC and lithostatic pressure of 1.3 GPa, in order to match the inferred conditions of brittle deformation in the studied Patagonian sample. Hence, we assume that dislocation creep, $\dot{\varepsilon}_{dis}$, is the only mechanism of viscous deformation, $\dot{\varepsilon}_{visc}$, in the model:

$$\dot{\varepsilon}_{visc} = \dot{\varepsilon}_{dis} = A\tau_{II}^{n} exp\left(\frac{-Q}{RT}\right) \quad (1)$$

where $A, n$ and $Q$ are dislocation creep constants, $R$ is the universal gas constant, $\tau_{II}$ is the square root of the second invariant of the deviatoric stress tensor, and $T$ is the temperature.

We use the Drucker-Prager criterion for plasticity:

$$\tau_y = C \cdot cos\alpha + P \cdot (1 - \lambda) \cdot sin\alpha \quad (2)$$

$$P = P_{lith} + P_{dyn} \quad (3)$$

$$\lambda = \frac{P_f}{P_{lith}} \quad (4)$$

where $\tau_y$ is the yield strength, $C$ is the cohesion, $\mu$ is the coefficient of friction (30º for both phases), $P$ is the total pressure, $\lambda$ is the pore fluid pressure ratio, $P_{lith}$ is the lithostatic pressure, $P_{dyn}$ is the dynamic pressure, and $P_f$ is the pore pressure. All rheological properties of matrix and garnet are described in Table 1.

### 4.2 Model setup

We use fixed boundary at the bottom, open boundaries at the sides, and kinematic boundary with horizontal velocity, $v$, at the top. Velocity, $v$, at the top is chosen to reproduce particular bulk shear strain rate $\dot{\gamma}$:

$$v = \dot{\gamma} \cdot h \quad (5)$$

where $h$ is the model's depth (50 mm).

As garnet crystals move to the right direction during the run of the model, we do not add new garnets. The final state of the model is achieved after bulk shear strain $\gamma$ reaches a value of 1, i.e., a displacement of the top boundary by 50 mm. At the final state, the model includes empty space in the form of a triangle at the left side of the model. In this way, we observe deformations of the model only in the right half of the model (the range of x axis from 0 to 50 mm) which is framed with a green dashed line in Figure 3b.

### 4.3 Styles of deformation

In this study, we explore the parameter space of the bulk shear strain rate, $\dot{\gamma}$, and pore fluid pressure ratio, $\lambda$. We vary the bulk shear strain rate, $\dot{\gamma}$, in the range between $10^{-15}$ and $10^{-4}$ 1/s which are representative of typical deep subduction interface strain rates. Although it is widely accepted that the pore fluid pressure ratio, $\lambda$, in subduction interface varies in the range 0.9 – 0.99 (Sobolev & Babeyko, 2005; Lamb, 2006; Moreno et al., 2014; Angiboust et al., 2015), we vary $\lambda$ from 0.37 (hydrostatic pressure) to 0.995 to cover all possible cases.

We classify models by their stress state; for this, we introduce the parameter of normalized stress $\sigma_{norm}$, which is equal to the ratio of the average shear stress on the top of the model (approximated by the square root of the second invariant of the deviatoric stress tensor, $\tau_{II}$) and the theoretical yield strength of the material (Equation 2):

$\sigma_{norm} = \tau_{II}/\tau_y$ (6)

Note that this parameter cannot be higher than 1. In this way, along with observations of the style of deformation in the model, we track the evolution of the normalized stress over the shear strain (Figure 4a).

Since garnet crystals cannot cross the kinematic boundary of the model, the average shear stress on the top of the model mostly characterizes the state of the quartzite matrix. In the beginning of the simulation, when there is no elastic stress in the model, shearing results in elastic loading of the model. Later, stress reaches peak value and remains relatively constant

(Figure 4a). The peak value depends on the style of deformation inside the model. We distinguish 4 styles of deformation (Figure 4b). For the sake of clarity and simplicity, in Figure 4 we only show models with $\lambda = 0.75$ and bulk shear strain rate, $\dot{\gamma}$, of $10^{-12}$, $10^{-10}$, $10^{-9}$, and $10^{-7.5}$ 1/s, which however cover the whole range of deformation styles observed in the models.

The first style is characterized by the absence of any frictional deformation (Style 1 in Figure 4b). While the matrix deforms in a viscous way, garnet crystals remain undeformed. However, shearing of the model results in rotation of the garnet crystals. Notably, the highest strain rate is observed in the vicinity of garnet crystals, especially those closer to other garnets (in line with earlier observations by Kenkmann & Dresen, 1998, and more recent results by Vriejmoed & Podladchikov, 2015). Since there is no frictional deformation, peak shear stress on the top surface is below yield strength (Equation 2) and regulated by the viscous parameters of matrix, temperature and bulk shear strain rate. In this way, friction of the matrix and garnet crystals as well as pore fluid pressure have no effect on stress in the model.

The second style (Style 2 in Figure 4b) is similar to the first one, with the difference that frictional deformation appears on the rims of garnet crystals. Nevertheless, even though frictional deformation is present, we cannot exclude that its occurrence is a numerical artifact, and in this case, the second style would become the same as the first one. Since in our models we use regular quadratic mesh, elements on the borders of circular garnets contain markers of both materials (inset of Figure 3a). Existence of both types of markers in one element results in the averaging of rheological properties of that element and leads to localization of stresses and subsequently frictional deformation (e.g., Ioannidi et al., 2022).

In the models of the third style (Style 3 in Figure 4b) frictional deformation occurs inside the garnet crystals, while the matrix remains viscous. In these models, garnet crystals both deform frictionally and rotate. The peak value of the stress on the top surface stays below yield strength due to the ability of the matrix to release stress load in the form of viscous deformation. However, garnet crystals which do not deform viscously at 550 ºC eventually accumulate stress at the level of yielding and deform plastically.

Finally, the fourth style (Style 4 in Figure 4b) is characterized by frictional deformation inside of the whole model. During shearing of the model there is no rotation of the garnets. Plots of plastic strain and strain rate show flat-lying, parallel shear bands across the model. Although the whole model deforms plastically, there is still some component of viscous deformation in the matrix, which results in a negligible difference in the accumulated plastic strain between matrix and garnet crystals.

### 4.4 Effect of shear strain rate and pore fluid pressure

To decipher the connection between the styles of deformation and normalized stress, we map the normalized stress as a function of the pore fluid pressure ratio, $\lambda$, and the bulk shear strain rate, $\dot{\gamma}$, with isolines separating the different styles of deformation, which are given by the markers (Figure 5). To underline the behavior of our models at very high pore fluid pressure ratios (typical for subduction zones), we separate our results into two sub-figures: Figure 5a on the left shows the normalized stresses for relatively low pore fluid pressure ratios (from hydrostatic conditions to $\lambda = 0.90$) and faster strain rates ($10^{-12}$ to $10^{-6}$ 1/s); Figure 5b on the right shows the normalized stresses for high pore fluid pressure ratios ($\lambda \geq 0.95$) and lower strain rates ($10^{-15}$ to $10^{-9}$ 1/s).

At low pore fluid pressure ratios (Figure 5a) and low strain rates, all models deform viscously (Style 1 and to some extent Style 2 in Figure 4b). As either strain rates or pore fluid pressures increase, shearing of the sample is accommodated by frictional failure in garnet, while the matrix remains viscous (Style 3). Finally, when strain rate is above $10^{-7}$ 1/s, pore fluid pressure does not play a role in the type of deformation; strain rate is high enough that both minerals deform frictionally (Figure 5a and Style 4 in Figure 4b). The white lines in Figure 5 denote the aforementioned transitions between deformation styles and show a clear dependency on pore fluid pressure and strain rate. Notably, strain rates that promote frictional failure in the models (Style 3 and 4) can vary up to two orders of magnitude for the different pore pressures examined here.

When pore fluid pressure ratios are very elevated ($\lambda \geq 0.95$; Figure 5b), deformation depends less on $\lambda$, as attested by the almost horizontal white lines, and more on strain rate. The lowest strain rates produce viscous deformation (Style 1 and 2), while for $\dot{\gamma}$ >$10^{-12.5}$ 1/s, frictional-viscous (Style 3) and frictional (Style 4) deformation prevails in the models. It is important to note that even though we prescribe a background strain rate, locally the strain rate may increase up to a few orders of magnitude inside the model (see right column of Figure 4b).

Interestingly, models with the same style of deformation appear in the fixed range of normalized stress regardless of their $\lambda$ and $\dot{\gamma}$: Style 1 appears in the range [0, ~0.2], Style 2 appears in the range [~0.2, ~0.5], Style 3 appears in the range [~0.5, ~0.99], and Style 4 appears only when $\sigma_{norm}$ is 1. It should be noted, however, that there is some overlap in the $\sigma_{norm}$ values between Style 1 and 2 (thick white line in high $\lambda$ models), and Style 2 and 3 (thick white line in low $\lambda$ models). The aforementioned overlap occurs due to our strict approach in style definition. For example, for a model to be classified as Style 2, it must have at least one element with non-zero plastic deformation on the rim of the garnet crystal but no elements with plastic deformation anywhere else inside of the observation area at the end of the simulation. However, models with different pore fluid pressures and shear strain rates but with equal peak stresses might reach peak stress at slightly different strains. This leads to different relative positions of garnet crystals at the moment when they reach peak stress, which consequently varies the stress field inside of the model and might cause yielding. Tables A1 and A2 provide all the values used for creating Figure 5.

# 5. DISCUSSION

## 5.1 Limitations of the numerical models

We have assumed a bi-mineralic composition (garnet and quartz) for the numerical models, even though exhumed rocks show a more complex composition with minor amounts of other phases such as white mica, amphibole, albite or epidote. However, the inclusion of more phases would increase the complexity of the model and would make interpretation of the results impossible. Moreover, garnet is the mineral in the assemblage which shows the more distinct microstructural characteristics of fracturing. We therefore focus our modelling investigations on this phase, even though a higher ratio of strong phases (e.g., competent/brittle feldspar crystals) can significantly influence the rheology of the modelled assemblage (Yamato et al., 2019; Beall et al., 2019a,b; Ioannidi et al., 2021; Rogowitz et al., 2022).

Also, our stress estimates apply for temperature-depth conditions (T>500°C, depth>30-40 km) where dislocation creep dominates over other deformation mechanisms (including pressure solution creep, PSC). Even though PSC is an important mechanism in subduction zone rocks at shallower depths (15-30 km e.g., Stöckhert, 2002; Fagereng and Den Hartog, 2017), it occurs mostly as a late process in our samples and related with vertical shortening and duplex-forming processes (e.g. Richter et al., 2007). In any case, PSC could not be modeled here due to the imprecision of available flow laws for high temperature conditions. We therefore consider dislocation creep as the only viscous mechanism for both minerals at 1.3 GPa and 550 °C. Nonetheless, the evaluation of stresses in the matrix based only on quartz dislocation creep flow law should be considered as an upper bound (e.g., Wallace et al., 2012; Smye & England, 2023 and references therein). This is because (i) deformation via PSC is known to occur at lower stresses than those necessary for activating dislocation creep, and (ii) the white mica in the matrix foliation would likely accommodate part of the total plastic strain. In addition, there exist uncertainties in the dislocation creep parameters ($A, n, Q$) derived from laboratory experiments. Therefore, although the succession of the deformation styles would remain the same for different creep parameters, the absolute values of strain rates and stresses may vary to some extent. For the sake of clarity, in this manuscript, we consider low strain rates values ≤ $10^{-11}$ 1/s and high values ≥ $10^{-7}$ 1/s; values in between are then referred to as moderate (typically $10^{-8}$ 1/s).

Finally, due to the nature of our numerical approach (FEM is a continuum mechanics formulation), it is not possible for the material to fracture, creating new interfaces. Therefore, frictional deformation is approximated by flow instead of spatial discontinuity (fracturing). As a consequence, garnet crystals do not fracture but become elongated towards the shearing direction and consequently remain apparently bounded to the original crystal in these sheared domains. Note that a similar macroscopic pattern has been reported in cataclastically-deformed garnet crystals from the high-pressure Sesia zone in the Italian Alps (Trepmann & Stöckhert, 2002).

### 5.2 Comparison with previous studies

Numerous mechanical studies have investigated the rheology of two-phase rock assemblages, experimentally (e.g., Ji et al., 2000; Jin et al., 2001; Rybacki et al., 2003), numerically (Kenkmann & Dresen, 1998; Beall et al., 2019a,b; Yamato et al., 2019; Ioannidi et al., 2021; 2022; Rogowitz et al., 2023), theoretically (e.g., Huet et al., 2014), or using natural samples (Handy et al., 1990; Grigull et al., 2012). Most garnet porphyroclasts studied previously were metamorphosed under eclogite facies conditions (Yamato et al., 2019; Rogowitz et al., 2023) and hence are embedded in an omphacite-bearing matrix, the rheology of which is much stronger than quartz as for our experiment. A stronger matrix would enable the accumulation of stresses sufficient to produce deformation within the clast under a lower strain rate rather than in the weak matrix (e.g., Beall et al., 2019a; Ioannidi et al., 2022). Yamato et al. (2019) found that locally increased stresses at the grain boundaries of garnet crystals can reach their yield strength and cause frictional failure; this deformation might be analogous to our Style 2 deformation. Moreover, varying volume fractions of garnet crystals would also result in varying the rheological behavior of the eclogite. This is also supported by Rogowitz et al. (2023) who studied omphacite-garnet assemblages (experimentally and numerically) and reported that larger fractions of garnet crystals resulted in higher strain localization in their samples. The high garnet-content models of both studies would correspond to the load-bearing framework of Handy (1990) where the strength of the aggregate depends primarily on that of the strong constituent phase. In our study, however, the garnet content is low (10%), therefore a load-bearing framework is never achieved. Instead, our numerical rock assemblage shows characteristics of either a clast-in-matrix (Style 1 and 2) or a boudin-matrix rheology (Style 3), according to the classification by Handy (1990). Rogowitz et al. (2023) also reported the co-existence of both frictional and viscous (dislocation creep) features in the garnet crystals. In our models, we do not observe any viscous deformation of the garnet crystals, even in Style 1, where there is no frictional/plastic deformation either. The difference between our results and those of Rogowitz et al. (2023) mostly arise due to the lower PT conditions of our experiment compared to their models (1000°C and 2.5 GPa, respectively).

### 5.3 Garnet as a witness of ancient unstable slip events

While fractured, decapitated or truncated porphyroclasts are a common feature in strained metamorphic rocks, estimating the strain rates that led to these microstructures is a challenging task (e.g., Küster & Stöckhert, 1999; Johnson et al., 2021). Garnet fracturing as a record of co-seismic deformation has been proposed in pseudotachylyte-bearing mylonitic gneisses, i.e., in material that slipped at seismic strain rates during metamorphism in the granulite facies (e.g. Austrheim et al., 1996; Hawemann et al., 2019). Trepmann & Stöckhert (2002) use the presence of fractured and offset garnet crystals as a marker of syn-seismic loading and subsequent post-seismic creep. However, it is clear that not all healed fractures in garnet should be interpreted in terms of unstable, fast-slip events. Fracturing of garnet has been reported in retrogressed metamorphic rocks undergoing exhumation-related deformation (e.g. Ji et al., 1997; Giuntoli et al., 2017). Other processes such as crystal indentation and crack-tip propagation during ductile shearing can locally lead to sufficiently high stresses to reach the garnet brittle envelope (e.g., Prior, 1993). Numerical simulations by Yamato et al. (2019) have revealed that whole-rock shearing of an eclogite at moderate strain rates (for instance $10^{-8}$ 1/s) can generate garnet rupture without involving seismic slip rates. Unlike these previous experiments, we deal here with two phases which exhibit an extreme viscosity contrast (more than 5 orders of magnitude at 550°C). Our numerical results indicate that when a quartz-rich/garnet-poor matrix is affected by shearing, the only possibility for having garnet crystals to break without any rotation is to have the formation of localized, foliation-parallel bands in which both the matrix and the clasts behave in a brittle fashion (Style 4). This pattern may occur for strain rates covering a range from slow earthquakes to just before the onset of long-term creep (Oncken et al., 2022), depending on the pore fluid pressure ratio (Fig.5).

Garnet fracturing in HP metasediments is rarely documented in exhumed suture zones and most garnet morphologies appear undisturbed in their major element zoning patterns. The pervasive fracturing of solitary garnet crystals in a quartzo-micaceous matrix as observed in Diego de Almagro Puerto Shear Zone samples thus points to anomalous conditions with respect to standard subduction slab-top environments. Nearly-lithostatic pore fluid pressure is expected for all deep SZ settings as demonstrated in numerous geophysical and geological studies (Peacock et al., 2011; Angiboust et al., 2015; Condit & French, 2022). It is thus inferred from our numerical investigations that acceleration of strain rate from standard subduction zones conditions ($10^{-12}$ 1/s) to localized, 'faster' slip conditions (from $10^{-11}$ or $10^{-10}$ 1/s for high $\lambda$ values to higher than $10^{-4}$ 1/s for lower $\lambda$ values) is required to trigger the deformation pattern depicted in Style 4, namely, the cataclasis of the rock volume (Fig.6a). While the earlier 'slow' deforming conditions can easily be envisioned during interseismic creeping between two slip events, the latter 'faster' conditions might correspond in nature to accelerated slip rate, for instance during post-seismic relaxation or SSEs (Fig.6).

From these observations, we can propose that the studied sample corresponds to a (cryptic) cataclasite which has been later foliated upon slip rate deceleration (and subsequent exhumation-related dynamic recrystallization; see also Sibson, 1980). Given the size of fractured fragments (several hundreds of microns in diameter; see Appendix), it is clear that the fracturing of the studied sample has not occurred in a fault core itself (gouge) where hundred-times smaller fragments are expected (Johnson et al., 2021). So, what happened with the fault core? One possibility is that its extremely fine-grained nature has caused the total replacement of the matrix during exhumation-related re-equilibration.

Last, the thermal gradient at the time of brecciation was elevated (c.12°C/km; Angiboust et al., 2018) and likely representative of a warm subduction regime similar to the one that can presently be observed in Nankai or Cascades interfaces (Peacock, 1996). Because such young subducted plates are characterized by a well-defined downdip limit of megathrust earthquakes at near 350°C, well-above the upper plate Moho (Oleskevich et al., 1999), we speculate that the observed paleoseismicity does not directly reflect the propagation of a megathrust rupture down to c.45 km depth (i.e. at studied fracturing conditions). Instead, this depth corresponds in warm active margins to the region affected by slow earthquakes (e.g. Bassett et al., 2022; Fig.6b), inferred to occur on the interface itself (so, probably in a sedimentary-rich environment).

We conclude emphasizing that (i) the foliated cataclasite herein studied could record some of the transient creep events associated with slow slip event phenomena (in line with Oncken et al., 2022) and that (ii) cataclasis and brittle creep (in the sense of Brantut et al., 2013) should be viewed as a prevalent deformation mechanism operating in deep, fluid-rich, subduction fault systems (and not restricted to shallow crustal conditions as classically envisioned in rheological profiles).

## 6. CONCLUSIONS

We have presented 2D numerical models that shed light on fracturing and viscous deformation of a high-pressure, bi-mineralic block-in-matrix assemblage, composed of garnet within a quarzitic matrix. Our results show that the style of deformation depends on the ratio of the stress in the matrix and its yield strength (namely the normalized stress), which is modulated by strain rate and pore fluid pressure ratio. Higher strain rate and higher pore fluid pressure ratio favor high stress in the model. For fixed pore fluid pressure conditions and for slow strain rates, minor clast rotation and distributed matrix deformation are observed. As strain rate increases, garnet becomes brittle, and instead of rotating, it develops internal shear bands which lead to its fracturing, while the matrix remains viscous. Finally, at the fastest strain rates, both matrix and garnet fracture, with distinct shear bands forming throughout the model. The latter pattern can explain the pervasively fractured garnet crystals found in a metasediment exhumed from the former Patagonian subduction interface where 'lost' fast-slipping events (i.e. via conventional earthquakes or more likely, slow earthquakes) probably took place via cataclastic flow. Our study calls for a re-appraisal of cryptic microstructures in garnet-bearing metasediments that are likely to have hosted unstable slip events along ancient tectonic plate boundary settings.

## ACKNOWLEDGMENTS

O. Oncken, T. Hyppolito and J. Muñoz-Montecinos are acknowledged for insightful discussions and assistance in the field.

## REFERENCES CITED *(68)*

Angiboust, S., Menant, A., Gerya, T., & Oncken, O. (2022). The rise and demise of deep accretionary wedges: A long-term field and numerical modeling perspective. Geosphere, 18(1), 69-103.

Angiboust, S., Cambeses, A., Hyppolito, T., Glodny, J., Monié, P., Calderón, M., & Juliani, C. (2018). A 100-my-long window onto mass-flow processes in the Patagonian Mesozoic subduction zone (Diego de Almagro Island, Chile). GSA Bulletin, 130(9-10), 1439-1456.

Angiboust, S., Kirsch, J., Oncken, O., Glodny, J., Monié, P., & Rybacki, E. (2015). Probing the transition between seismically coupled and decoupled segments along an ancient subduction interface. *Geochemistry, Geophysics, Geosystems*, *16*(6), 1905-1922.

Angiboust, S., Agard, P., Yamato, P., & Raimbourg, H. (2012). Eclogite breccias in a subducted ophiolite: A record of intermediate-depth earthquakes?. Geology, 40(8), 707-710.

Atkinson, B. K. (1984). Subcritical crack growth in geological materials. Journal of Geophysical Research: Solid Earth, 89(B6), 4077-4114.

Austrheim, H., & Andersen, T. B. (2004). Pseudotachylytes from Corsica: fossil earthquakes from a subduction complex. Terra nova, 16(4), 193-197.

Austrheim, H., Erambert, M., & Boundy, T. M. (1996). Garnets recording deep crustal earthquakes. Earth and Planetary Science Letters, 139(1-2), 223-238.

Bassett, D., Arnulf, A., Kodaira, S., Nakanishi, A., Harding, A., & Moore, G. (2022). Crustal structure of the Nankai subduction zone revealed by two decades of onshore-offshore and ocean-bottom seismic data: Implications for the dimensions and slip behavior of the seismogenic zone. *Journal of Geophysical Research: Solid Earth*, *127*(10), e2022JB024992.

Beall, A., Fagereng, Å., & Ellis, S. (2019). Strength of strained two-phase mixtures: Application to rapid creep and stress amplification in subduction zone mélange. *Geophysical Research Letters*, *46*(1), 169-178.

Beall, A., Fagereng, Å., & Ellis, S. (2019). Strength of strained two-phase mixtures: Application to rapid creep and stress amplification in subduction zone mélange. *Geophysical Research Letters*, *46*(1), 169-178.

Bebout, G. E., & Penniston-Dorland, S. C. (2016). Fluid and mass transfer at subduction interfaces—The field metamorphic record. Lithos, 240, 228-258.

Behr, W. M., & Bürgmann, R. (2021). What's down there? The structures, materials and environment of deep-seated slow slip and tremor. Philosophical Transactions of the Royal Society A, 379(2193), 20200218.

Brantut, N. et al. (2013) Time-dependent cracking and brittle creep in crustal rocks: A review. Journal of Structural Geology 52, 17-43.

Condit, C. B., French, M. E., Hayles, J. A., Yeung, L. Y., Chin, E. J., & Lee, C. T. A. (2022). Rheology of metasedimentary rocks at the base of the subduction seismogenic zone. Geochemistry, Geophysics, Geosystems, 23(2), e2021GC010194.

Condit, C. B., & French, M. E. (2022). Geologic evidence of lithostatic pore fluid pressures at the base of the subduction seismogenic zone. *Geophysical Research Letters*, *49*(12), e2022GL098862.

Fagereng, Å., & Den Hartog, S. A. (2017). Subduction megathrust creep governed by pressure solution and frictional–viscous flow. *Nature Geoscience*, *10*(1), 51-57.

Freymueller, J. T., Woodard, H., Cohen, S. C., Cross, R., Elliott, J., Larsen, C. F., ... & Ekström, G. (2008). Active deformation processes in Alaska, based on 15 years of GPS measurements. Active tectonics and seismic potential of Alaska, 179, 1-42.

Giuntoli, F., Lanari, P., & Engi, M. (2018). Deeply subducted continental fragments: I. Fracturing, dissolution-precipitation and diffusion processes recorded by garnet textures of the central Sesia Zone (Western Italian Alps). Solid Earth, 9, 167-189.

Gleason, G. C., & Tullis, J. (1995). A flow law for dislocation creep of quartz aggregates determined with the molten salt cell. Tectonophysics, 247(1-4), 1-23.

Grigull, S., Krohe, A., Moos, C., Wassmann, S., & Stöckhert, B. (2012). "Order from chaos": a field-based estimate on bulk rheology of tectonic mélanges formed in subduction zones. Tectonophysics, 568, 86-101.

Hacker, B. R., Peacock, S. M., Abers, G. A., & Holloway, S. D. (2003). Subduction factory 2. Are intermediate-depth earthquakes in subducting slabs linked to metamorphic dehydration reactions?. Journal of Geophysical Research: Solid Earth, 108(B1).

Handy, M. R. (1990). The solid-state flow of polymineralic rocks. *Journal of Geophysical Research: Solid Earth*, *95*(B6), 8647-8661.

Hawemann, F., Mancktelow, N., Wex, S., Pennacchioni, G., & Camacho, A. (2019). Fracturing and crystal plastic behaviour of garnet under seismic stress in the dry lower continental crust (Musgrave Ranges, Central Australia). Solid Earth, 10(5), 1635-1649.

Hervé, F., & Fanning, C. M. (2003). Early Cretaceous subduction of continental crust at the Diego de Almagro archipelago, southern Chile. Episodes Journal of International Geoscience, 26(4), 285-289.

Huet, B., Yamato, P., & Grasemann, B. (2014). The Minimized Power Geometric model: An analytical mixing model for calculating polyphase rock viscosities consistent with experimental data. Journal of Geophysical Research: Solid Earth, 119(4), 3897-3924.

Hyppolito, T., Angiboust, S., Juliani, C., Glodny, J., Garcia-Casco, A., Calderón, M., & Chopin, C. (2016). Eclogite-, amphibolite-and blueschist-facies rocks from Diego de Almagro Island (Patagonia): Episodic accretion and thermal evolution of the Chilean subduction interface during the Cretaceous. Lithos, 264, 422-440.

Hyppolito, T., Cambeses, A., Angiboust, S., Raimondo, T., García-Casco, A., & Juliani, C. (2019). Rehydration of eclogites and garnet-replacement processes during exhumation in the amphibolite facies. Geological Society, London, Special Publications, 478(1), 217-239.

Incel, S., Hilairet, N., Labrousse, L., John, T., Deldicque, D., Ferrand, T., ... & Schubnel, A. (2017). Laboratory earthquakes triggered during eclogitization of lawsonite-bearing blueschist. Earth and Planetary Science Letters, 459, 320-331.

Ioannidi, P. I., Le Pourhiet, L., Agard, P., Angiboust, S., & Oncken, O. (2021). Effective rheology of a two-phase subduction shear zone: Insights from numerical simple shear experiments and implications for subduction zone interfaces. *Earth and Planetary Science Letters*, *566*, 116913.

Ioannidi, P. I., Bogatz, K., & Reber, J. E. (2022). The Impact of Matrix Rheology on Stress Concentration in Embedded Brittle Clasts. Geochemistry, Geophysics, Geosystems, 23(3), 1–19. https://doi.org/10.1029/2021gc010127

Ji, S., Zhao, P., & Saruwatari, K. (1997). Fracturing of garnet crystals in anisotropic metamorphic rocks during uplift. Journal of Structural Geology, 19(5), 603-620.

Ji, S., & Martignole, J. (1994). Ductility of garnet as an indicator of extremely high temperature deformation. Journal of Structural Geology, 16(7), 985-996.

Jin, Z. M., Zhang, J., Green, H. W., & Jin, S. (2001). Eclogite rheology: Implications for subducted lithosphere. *Geology*, *29*(8), 667-670.

John, T., & Schenk, V. (2006). Interrelations between intermediate-depth earthquakes and fluid flow within subducting oceanic plates: Constraints from eclogite facies pseudotachylytes. Geology, 34(7), 557-560.

Johnson, S. E., Song, W. J., Vel, S. S., Song, B. R., & Gerbi, C. C. (2021). Energy partitioning, dynamic fragmentation, and off-fault damage in the earthquake source volume. Journal of Geophysical Research: Solid Earth, 126(11), e2021JB022616.

Kenkmann, T., & Dresen, G. (1998). Stress gradients around porphyroclasts: palaeopiezometric estimates and numerical modelling. *Journal of Structural Geology*, *20*(2-3), 163-173.

Kirkpatrick, J. D., & Rowe, C. D. (2013). Disappearing ink: How pseudotachylytes are lost from the rock record. Journal of Structural Geology, 52, 183-198.

Küster, M., & Stöckhert, B. (1999). High differential stress and sublithostatic pore fluid pressure in the ductile regime—microstructural evidence for short-term post-seismic creep in the Sesia Zone, Western Alps. Tectonophysics, 303(1-4), 263-277.

Lamb, S. (2006). Shear stresses on megathrusts: Implications for mountain building behind subduction zones, Journal of Geophysical Research, 111, B07401.

Lange, D., Tilmann, F., Barrientos, S. E., Contreras-Reyes, E., Methe, P., Moreno, M., ... & Beck, S. (2012). Aftershock seismicity of the 27 February 2010 Mw 8.8 Maule earthquake rupture zone. Earth and Planetary Science Letters, 317, 413-425.

Luo, H., & Wang, K. (2021). Postseismic geodetic signature of cold forearc mantle in subduction zones. Nature Geoscience, 14(2), 104-109.

Moreno, M., Haberland, C., Oncken, O., Rietbrock, A., Angiboust, S., & Heidbach, O. (2014). Locking of the Chile subduction zone controlled by fluid pressure before the 2010 earthquake. Nature Geoscience, 7(4), 292–296.

Muñoz-Montecinos, J., Angiboust, S., & Garcia-Casco, A. (2021). Blueschist-facies paleo-earthquakes in a serpentinite channel (Zagros suture, Iran) enlighten seismogenesis in Mariana-type subduction margins. Earth and Planetary Science Letters, 573, 117135.

Muñoz-Montecinos, J., Angiboust, S., Cambeses, A., & García-Casco, A. (2020). Multiple veining in a paleo–accretionary wedge: The metamorphic rock record of prograde dehydration and transient high pore-fluid pressures along the subduction interface (Western Series, central Chile). *Geosphere*, *16*(3), 765-786.

Oleskevich, D. A., Hyndman, R. D., & Wang, K. (1999). The updip and downdip limits to great subduction earthquakes: Thermal and structural models of Cascadia, south Alaska, SW Japan, and Chile. *Journal of Geophysical Research: Solid Earth*, *104*(B7), 14965-14991.

Oncken, O., Angiboust, S., & Dresen, G. (2022). Slow slip in subduction zones: Reconciling deformation fabrics with instrumental observations and laboratory results. Geosphere, 18(1), 104-129.

Passchier, C. W., Trouw, R. A. J., Zwart, H. J., & Vissers, R. L. M. (1992). Porphyroblast rotation: eppur si muove*?. Journal of Metamorphic Geology, 10(3), 283-294.

Peacock, S. M., Christensen, N. I., Bostock, M. G., & Audet, P. (2011). High pore pressures and porosity at 35 km depth in the Cascadia subduction zone. Geology, 39(5), 471-474.

Peacock, S. M. (1996). Thermal and petrologic structure of subduction zones. *Subduction: top to bottom*, *96*, 119-133.

Popov, A. A., & Sobolev, S. V. (2008). SLIM3D: A tool for three-dimensional thermomechanical modeling of lithospheric deformation with elasto-visco-plastic rheology. Physics of the Earth and Planetary Interiors, 171, 55– 75.

Prior, D. J. (1993). Sub-critical fracture and associated retrogression of garnet during mylonitic deformation. Contributions to Mineralogy and Petrology, 113(4), 545-556.

Richter, P. P., Ring, U., Willner, A. P., & Leiss, B. (2007). Structural contacts in subduction complexes and their tectonic significance: the Late Palaeozoic coastal accretionary wedge of central Chile. *Journal of the Geological Society*, *164*(1), 203-214.

Rogowitz, A., Thielmann, M., Kraus, K., Grasemann, B., & Renner, J. (2023). The effect of the garnet content on deformation mechanisms and weakening of eclogite: Insights from deformation

experiments and numerical simulations. Geochemistry, Geophysics, Geosystems, 24(3), e2022GC010743.
Rybacki, E., Paterson, M. S., Wirth, R., & Dresen, G. (2003). Rheology of calcite–quartz aggregates deformed to large strain in torsion. Journal of Geophysical Research: Solid Earth, 108(B2).

Shiina, T., Nakajima, J., & Matsuzawa, T. (2013). Seismic evidence for high pore pressures in the oceanic crust: Implications for fluid-related embrittlement. Geophysical Research Letters, 40(10), 2006-2010.

Sibson, R. H. (1980). Transient discontinuities in ductile shear zones. *Journal of Structural Geology*, *2*(1-2), 165-171.

Sippl, C., Schurr, B., Asch, G., & Kummerow, J. (2018). Seismicity structure of the northern Chile forearc from > 100,000 double-difference relocated hypocenters. Journal of Geophysical Research: Solid Earth, 123(5), 4063-4087.

Smye, A. J., & England, P. C. (2023). Metamorphism and deformation on subduction interfaces: 2. Petrological and tectonic implications. Geochemistry, Geophysics, Geosystems, 24(1), e2022GC010645.

Sobolev, S. V., & Babeyko, A. Y. (2005). What drives orogeny in the Andes? Geology, 33, 617– 620.

Stöckhert, B. (2002). Stress and deformation in subduction zones: insight from the record of exhumed metamorphic rocks. *Geological Society, London, Special Publications*, *200*(1), 255-274.

Trepmann, C. A., & Stöckhert, B. (2002). Cataclastic deformation of garnet: a record of synseismic loading and postseismic creep. Journal of Structural Geology, 24(11), 1845-1856.

Tulley, C. J., Fagereng, Å., & Ujiie, K. (2020). Hydrous oceanic crust hosts megathrust creep at low shear stresses. Science Advances, 6(22), eaba1529.

Vrijmoed, J. C., & Podladchikov, Y. Y. (2015). Thermodynamic equilibrium at heterogeneous pressure. Contributions to Mineralogy and Petrology, 170, 1-27.

Wallace, L. M., Fagereng, Å., & Ellis, S. (2012). Upper plate tectonic stress state may influence interseismic coupling on subduction megathrusts. Geology, 40(10), 895–898.

Wassmann, S., & Stoeckhert, B. (2013a). Rheology of the plate interface—Dissolution precipitation creep in high pressure metamorphic rocks. Tectonophysics, 608, 1-29.

Wassmann, S., & Stöckhert, B. (2013bwa). Low stress deformation of garnet by incongruent dissolution precipitation creep. Journal of Structural Geology, 46, 200-219.

Whitney, D. L., & Evans, B. W. (2010). Abbreviations for names of rock-forming minerals. American mineralogist, 95(1), 185-187.

Willner, A. P., Hervé, F., Thomson, S. N., & Massonne, H. J. (2004). Converging PT paths of Mesozoic HP-LT metamorphic units (Diego de Almagro Island, Southern Chile): evidence for juxtaposition during late shortening of an active continental margin. Mineralogy and Petrology, 81, 43-84.

Yamato, P., Duretz, T., & Angiboust, S. (2019). Brittle/ductile deformation of eclogites: insights from numerical models. Geochemistry, Geophysics, Geosystems, 20(7), 3116-3133.

## FIGURE & TABLE CAPTIONS

**Figure 1. Geological context of the studied sample. a** and **b**. Simplified geological map and cross-section showing the structure of the island comprising three main tectonic slivers

with peak pressure deformation ages of 165 Ma (Lazaro unit: brown), 130 Ma (Garnet amphibolite unit: green, from which the studied sample #47a indicated by yellow star comes from) and 80 Ma (Blueschist unit: BS: blue). PSZ: Puerto Shear Zone. **c**. Pressure-Temperature path followed by the studied sample (#47a) during Cretaceous burial-exhumation history (Hyppolito et al., 2016). The studied fracturing event occurred at near 120 Ma, 550°C and 1.3 GPa (approximately 45 km depth).

**Figure 2. Structure of studied garnet crystals. a.** Hand specimen photograph of the studied sample showing 1-3 mm sized garnet porphyroblasts in a foliated matrix comprising albite, phengite, amphibole, epidote and quartz. **b**. Optical microscope picture (plane polarized light, x2.5) showing a representative area of the sample. Abbreviations after Whitney and Evans (2010); C.M.: carbonaceous matter. **c** and **d**. X-ray maps showing the internal XMg (Mg/Mg+Fe) and Mn zoning structure of a large garnet crystal from sample #47a. Note the remarkable density of healed fractures as well as the dissolution of garnet right side marked with a white arrow on panel d. **e.** Scan of the studied thin section showing the garnet grains (Grt I cores have been colored in white for better visibility). **f** to **i**. BSE pictures showing the internal structure of garnet grains from the studied sample (see figure 2e for clast emplacement).

**Figure 3. Modeling – methodology**. **a.** Snapshot of material distribution at initial state with zoomed in area showing elements' mesh, where orange-beige checkerboard background denotes quartzite matrix and brown circles with black stripes denote garnets. **b.** Snapshot of the material distribution at the final state after achieving shear strain (γ) value of 1. Magenta dotted frame denotes projection of deformed profile and green dashed line denotes observation area with the size of 50 mm.

**Figure 4. Modeling - parameter exploration. a.** Evolution of the normalized stress over shear strain. **b.** In columns: material distribution, accumulated plastic strain, and strain rate at the final state of the models. Note that plastic strain in the second column refers to accumulated strain due to frictional deformation. In rows: Style 1 – no frictional deformation

in the whole model ($\dot{\gamma} = 10^{-12}\, 1/s$), Style 2 – frictional deformation only on the rims of the garnets ($\dot{\gamma} = 10^{-10}\, 1/s$), Style 3 – frictional deformation only inside of garnets ($\dot{\gamma} = 10^{-9}\, 1/s$), Style 4 – frictional deformation throughout the whole model ($\dot{\gamma} = 10^{-7.5}\, 1/s$).

**Figure 5. Modelling – Normal stress and deformation style. a.** Contour map of the normalized stresses of models with relatively high strain rates and low pore fluid pressure ratios. Markers denote the different deformation styles, while white lines mark the transition from one deformation style to another. **b.** Same as a, for lower strain rates and higher pore fluid pressure ratios. Note that even though we ran model up to $10^{-4}$ 1/s, the results between $10^{-6}$ and $10^{-4}$ 1/s are not displayed here as they show similar features over this range. **c**. Modified Mohr diagram where the shear stress in the y-axis has been replaced by the normalized stress (Equation 6). P corresponds to the total pressure (Equation 3). The inclined straight line denotes the rock failure envelope ($\sigma_{norm} = 1$). The homocentric circles denote the maximum calculated $\sigma_{norm}$ for the different deformation styles of our models. Grt stands for garnet, Qz for quartz.

**Figure 6**. **Conceptual figure**. **a.** Sketch depicting the influence of strain rate on the deformation style of garnet in our experiments. The conditions enabling the fracturing of garnet in a weak quarzitic matrix are met under relatively fast slip rates (possibly co-seismic) and extremely high pore fluid pressure conditions. **b**. Sketch of a subduction zone localizing the megathrust zone (red line), the slow slip events area (SSEs) and the location of the sample at the time of cataclasis (star). The inset shows a conceptual series of 5 seismic cycles and the corresponding deformation modes at each stage of the cycle.

**Table 1.** Rheological parameters for the materials used in the numerical models. Flow parameters for garnet are from Ji & Martignole (1994) and from Gleason & Tullis (1995) for quartz (matrix).

| | **Matrix** | **Garnet** |
|---|---|---|
| **Density ($kg/m^3$)** | 2800 | 3700 |
| **Shear modulus (GPa)** | 40.0 | 94.0 |
| **Bulk modulus (GPa)** | 63.0 | 171.0 |

| | | |
|---|---|---|
| **Cohesion (MPa)** | 50 | 50 |
| **Friction coefficient** | 30 | 30 |
| **Log(A) factor (1/Pa$^n$/s)** | -28.0 | -6.55 |
| **Activation energy (kJ/mol)** | 223 | 485 |
| **Exponent** | 4.0 | 2.22 |

**Appendix**:

- additional petrological data

- additional numerical modelling information (including tables A1 and A2)

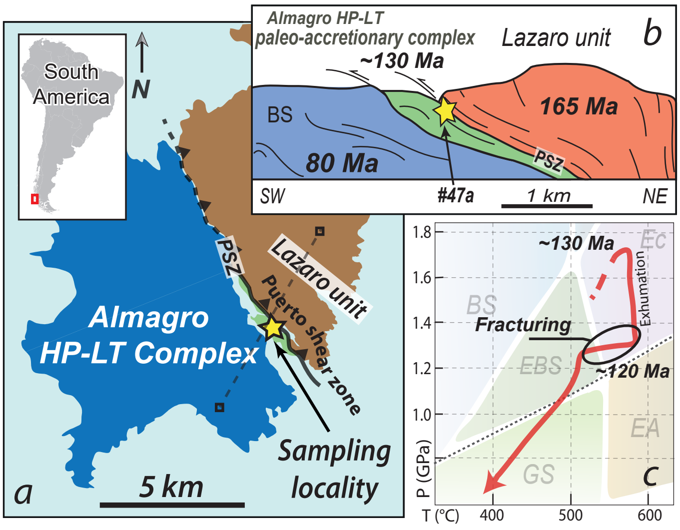
South America
N
Almagro HP-LT Complex
PSZ
Lazaro unit
Puerto shear zone
Sampling locality
5 km
a
Almagro HP-LT paleo-accretionary complex
Lazaro unit
b
~130 Ma
165 Ma
BS
80 Ma
PSZ
SW
#47a
1 km
NE
~130 Ma
Ec
BS
Fracturing
Exhumation
EBS
~120 Ma
EA
GS
c
P (GPa)
T (°C)
1.8
1.6
1.4
1.2
1.0
400
500
600

*Figure 1*

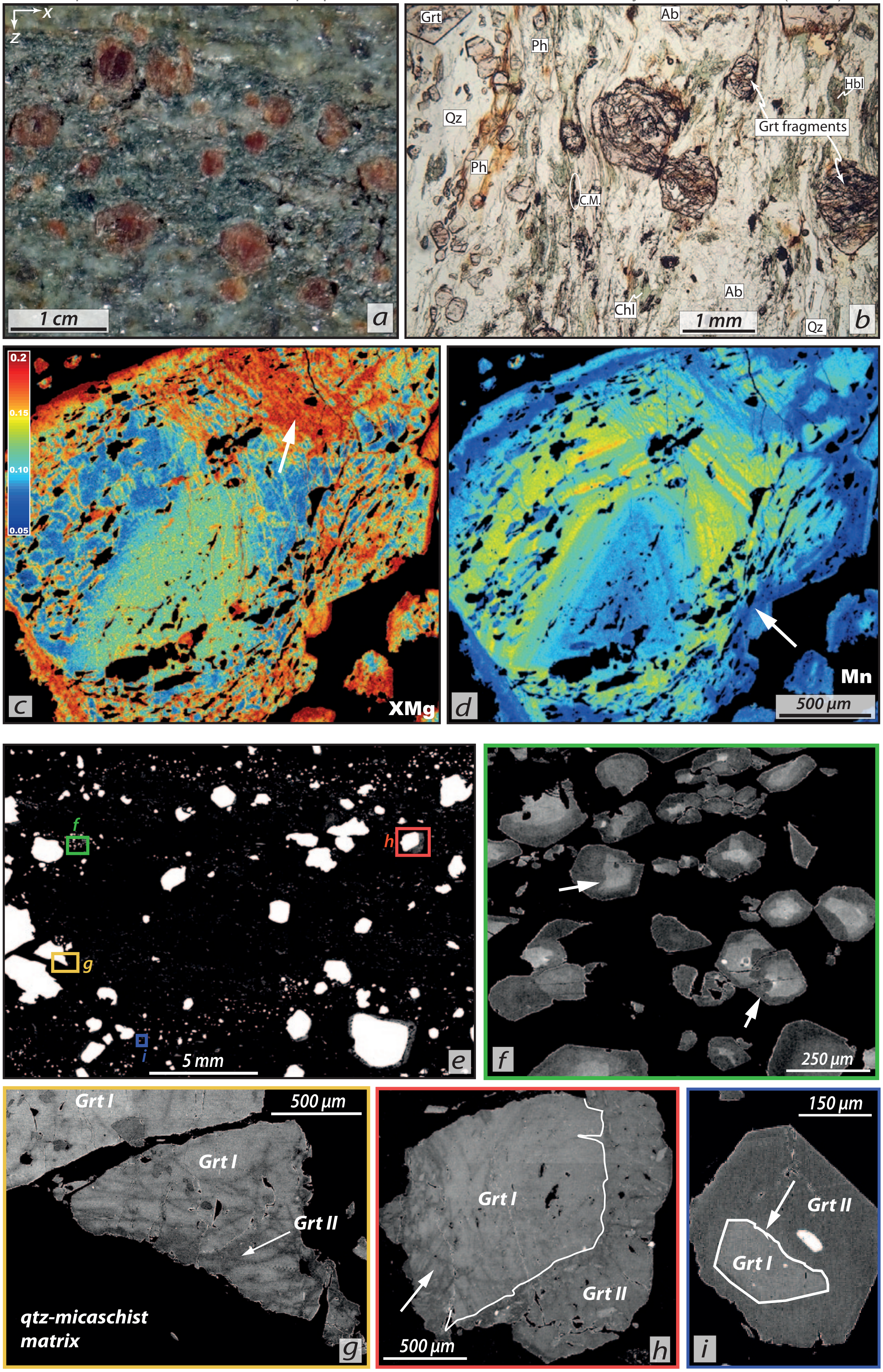
x
z
1 cm
a
Grt
Ab
Ph
Hbl
Qz
Grt fragments
Ph
C.M.
Ab
Chl
1 mm
Qz
b
0.2
0.15
0.10
0.05
c
XMg
Mn
d
500 µm
f
h
g
i
5 mm
e
f
250 µm
Grt I
500 µm
Grt I
Grt II
qtz-micaschist
matrix
g
Grt I
Grt II
500 µm
h
150 µm
Grt II
Grt I
i

Figure 2

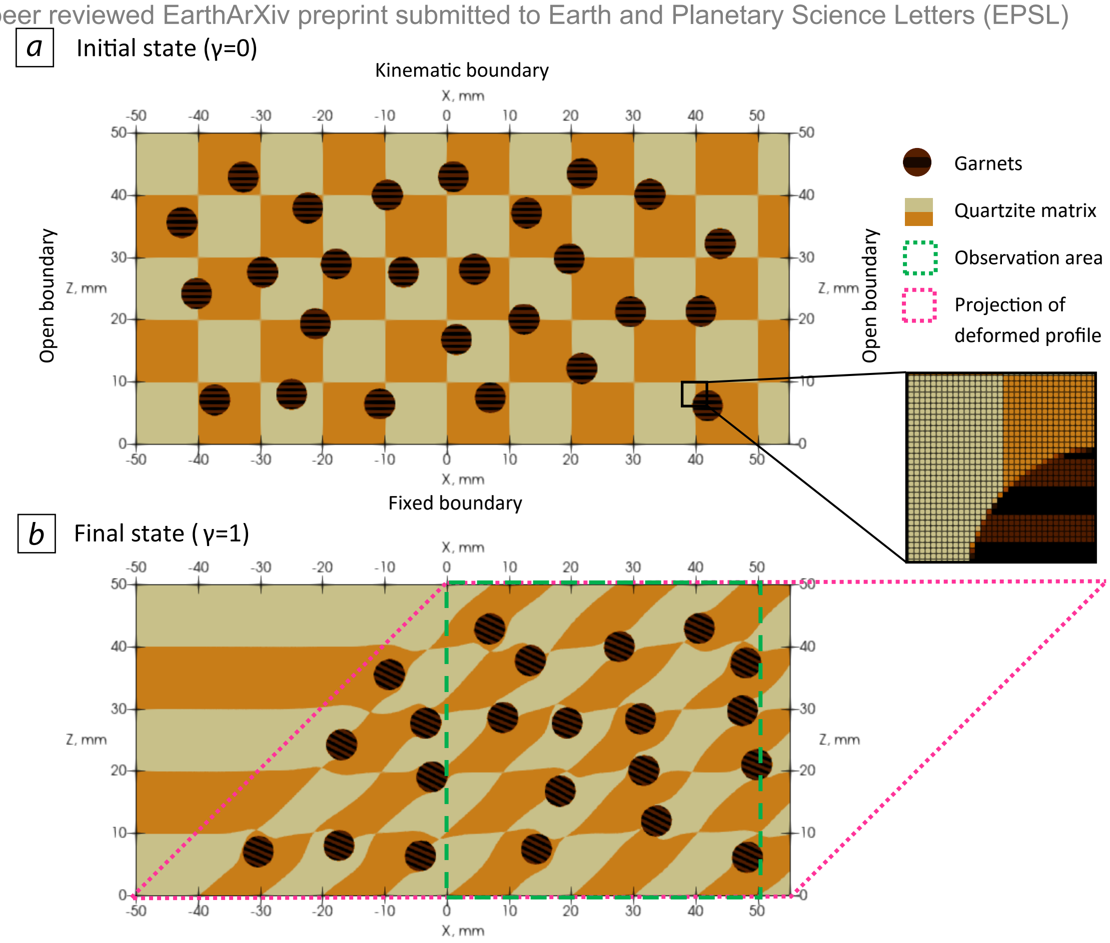
a
Initial state (γ=0)
Kinematic boundary
X, mm
-50
-40
-30
-20
-10
0
10
20
30
40
50
Z, mm
Open boundary
Open boundary
Fixed boundary
Garnets
Quartzite matrix
Observation area
Projection of
deformed profile
b
Final state ( γ=1)

*Figure 3*

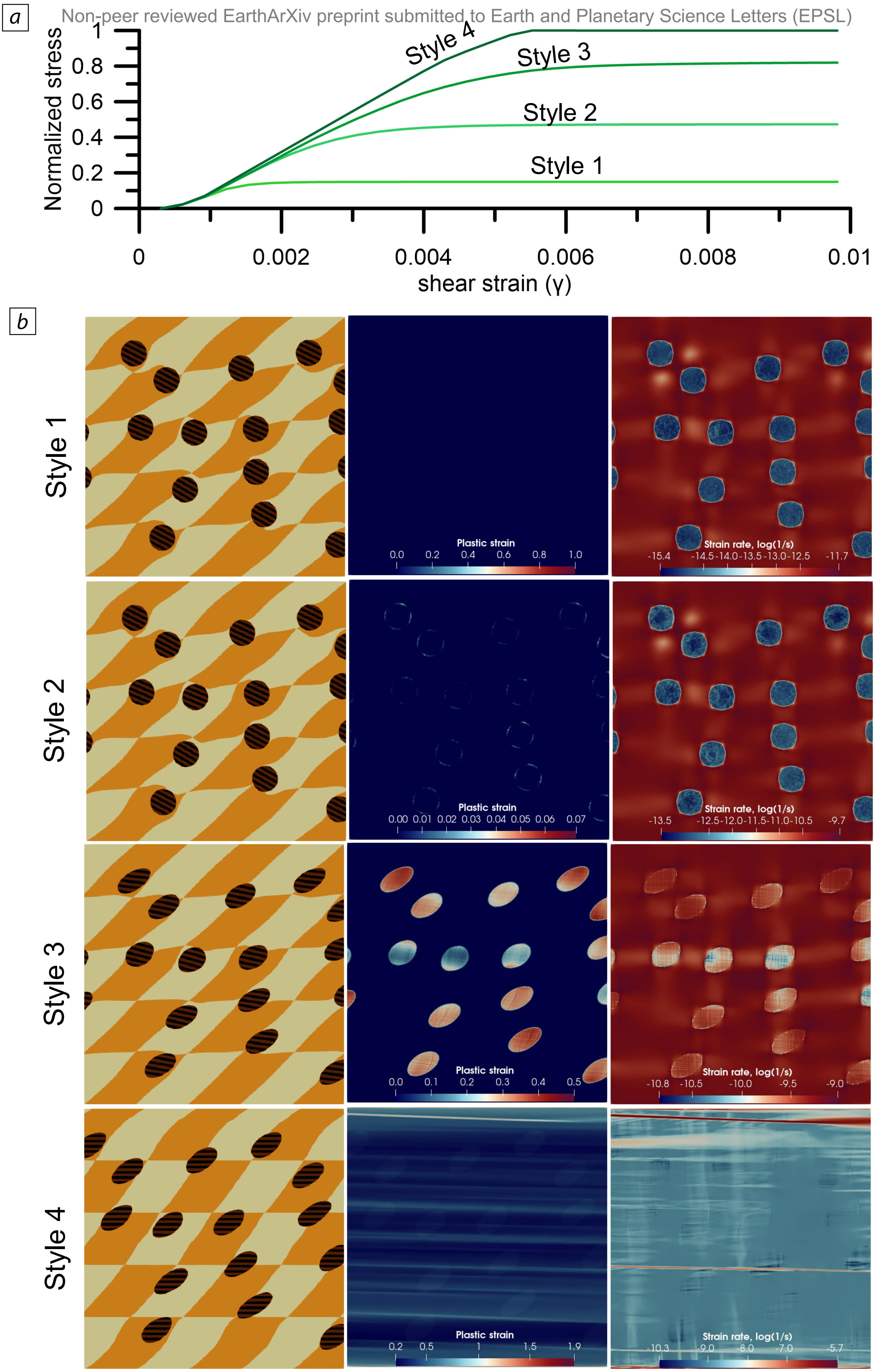
a
Normalized stress
0
0.2
0.4
0.6
0.8
1
Style 4
Style 3
Style 2
Style 1
0
0.002
0.004
0.006
0.008
0.01
shear strain (γ)
b
Style 1
Style 2
Style 3
Style 4
Plastic strain
Strain rate, log(1/s)

*Figure 4*

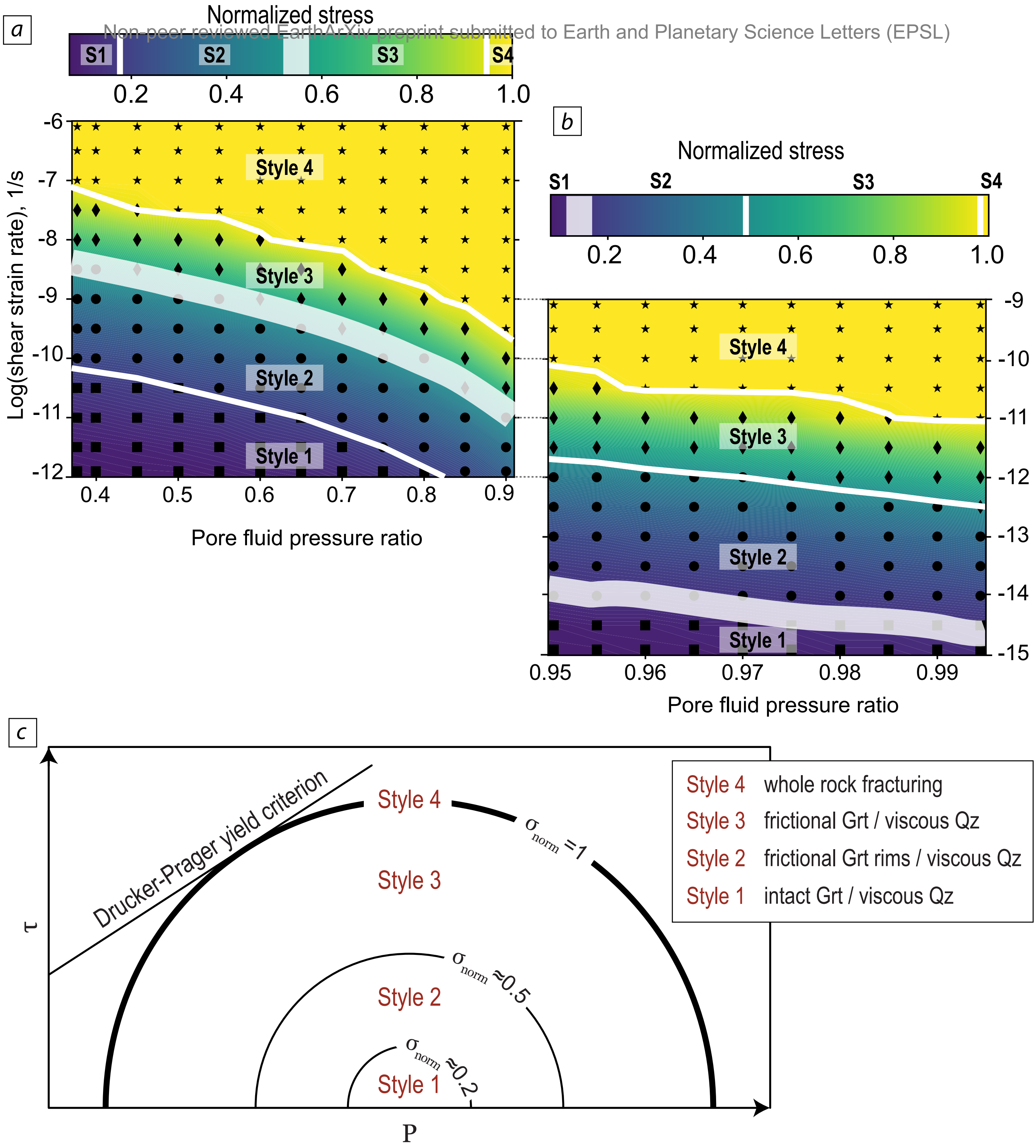
a
Normalized stress
S1
S2
S3
S4
0.2
0.4
0.6
0.8
1.0
Log(shear strain rate), 1/s
Style 4
Style 3
Style 2
Style 1
Pore fluid pressure ratio
b
Normalized stress
S1
S2
S3
S4
Style 4
Style 3
Style 2
Style 1
Pore fluid pressure ratio
c
Drucker-Prager yield criterion
Style 4
Style 3
Style 2
Style 1
σ norm =1
σ norm ≈0.5
σ norm ≈0.2
τ
P
Style 4 whole rock fracturing
Style 3 frictional Grt / viscous Qz
Style 2 frictional Grt rims / viscous Qz
Style 1 intact Grt / viscous Qz

*Figure 5*

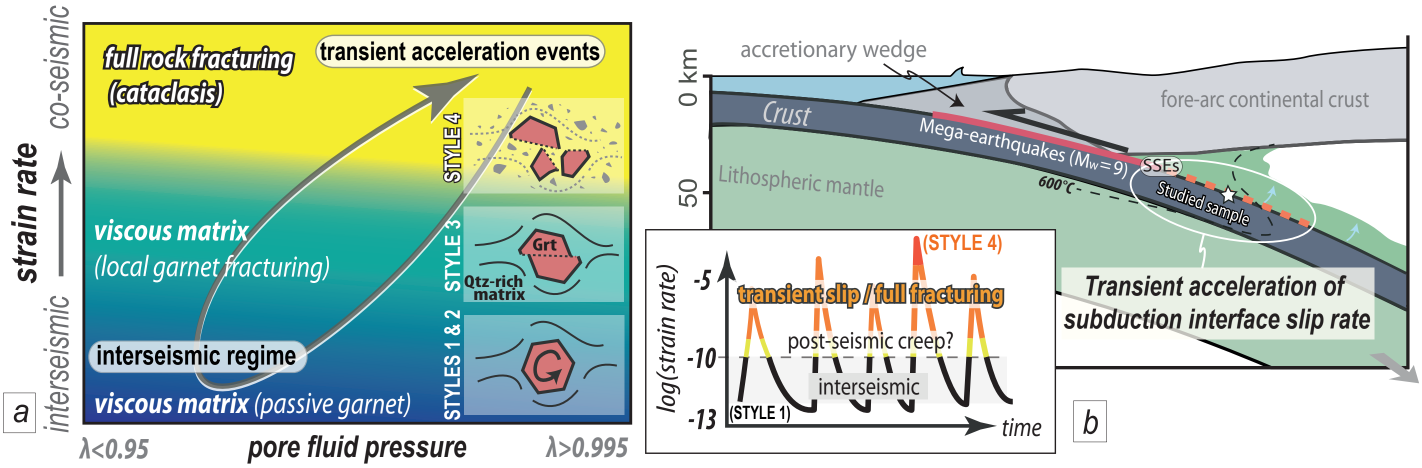
co-seismic
strain rate
interseismic
a
full rock fracturing
(cataclasis)
transient acceleration events
STYLE 4
viscous matrix
(local garnet fracturing)
STYLE 3
Grt
Qtz-rich matrix
interseismic regime
viscous matrix (passive garnet)
STYLES 1 & 2
λ<0.95
pore fluid pressure
λ>0.995
accretionary wedge
0 km
50
Crust
fore-arc continental crust
Mega-earthquakes (Mw=9)
SSEs
Lithospheric mantle
600°C
Studied sample
Transient acceleration of subduction interface slip rate
log(strain rate)
-5
-10
-13
(STYLE 4)
transient slip / full fracturing
post-seismic creep?
interseismic
(STYLE 1)
time
b

figure 6

# Appendix

## Analytical methods:

A scanning electron microscope (SEM) Zeiss EVO MA10 at the Institut de Physique du Globe de Paris using internal calibration standards was used for microstructural observations and mosaic imaging of the studied thin section. The electron probe x-ray maps were acquired at the GFZ Potsdam using a JEOL-JXA 8230 probe operated at 15 kV and 200 nA, with a beam size of 3 µm.

## Supplementary petrological material:

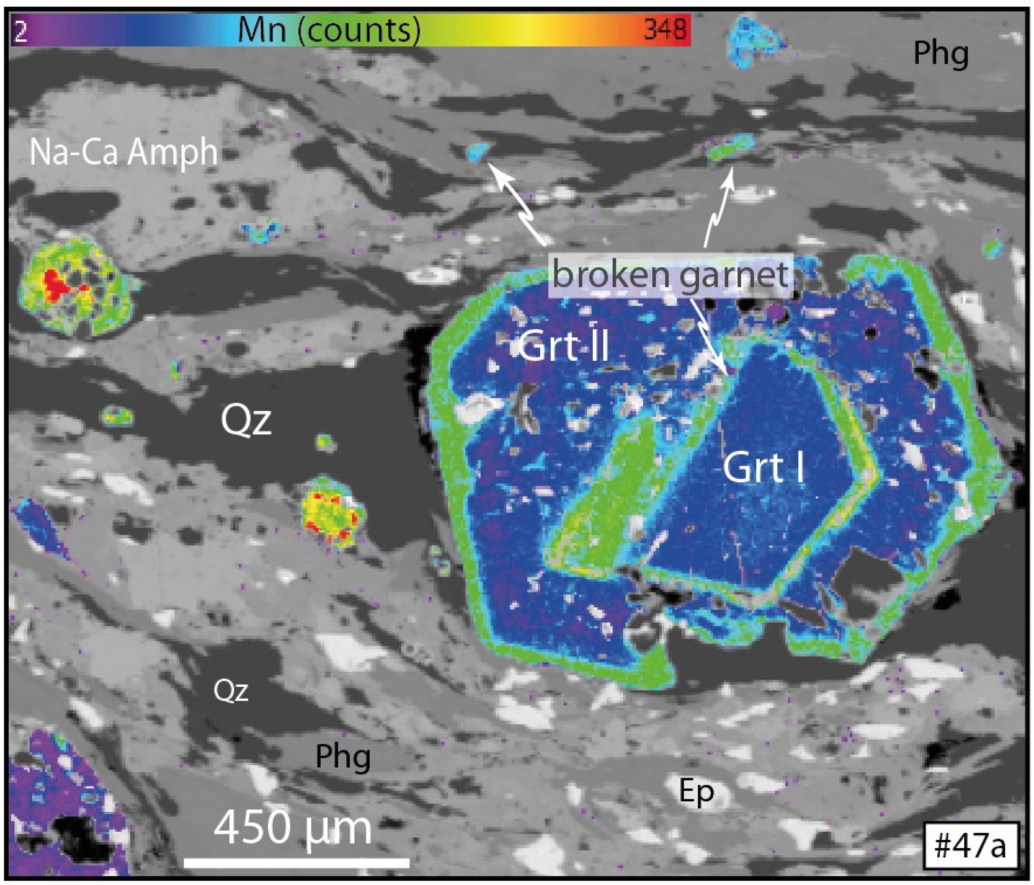


**Figure A.1**: X-ray map from a garnet porphyroclast from sample #47a showing the Mn content (in counts) of garnet crystals (BSE image as background). In this map, it is shown that garnet I got brecciated and has kept growing (Grt II) during metamorphic re-equilibration (amphibolite facies). Note the variably sized, xenomorphic garnet fragments dispersed along the foliation. Given their heterogeneous Mn content, we can infer that they represent remnants from various parts from former fractured garnet crystals that have been disseminated along the foliation upon post-fracturing shearing. Mineral abbreviations after Whitney & Evans (2010).

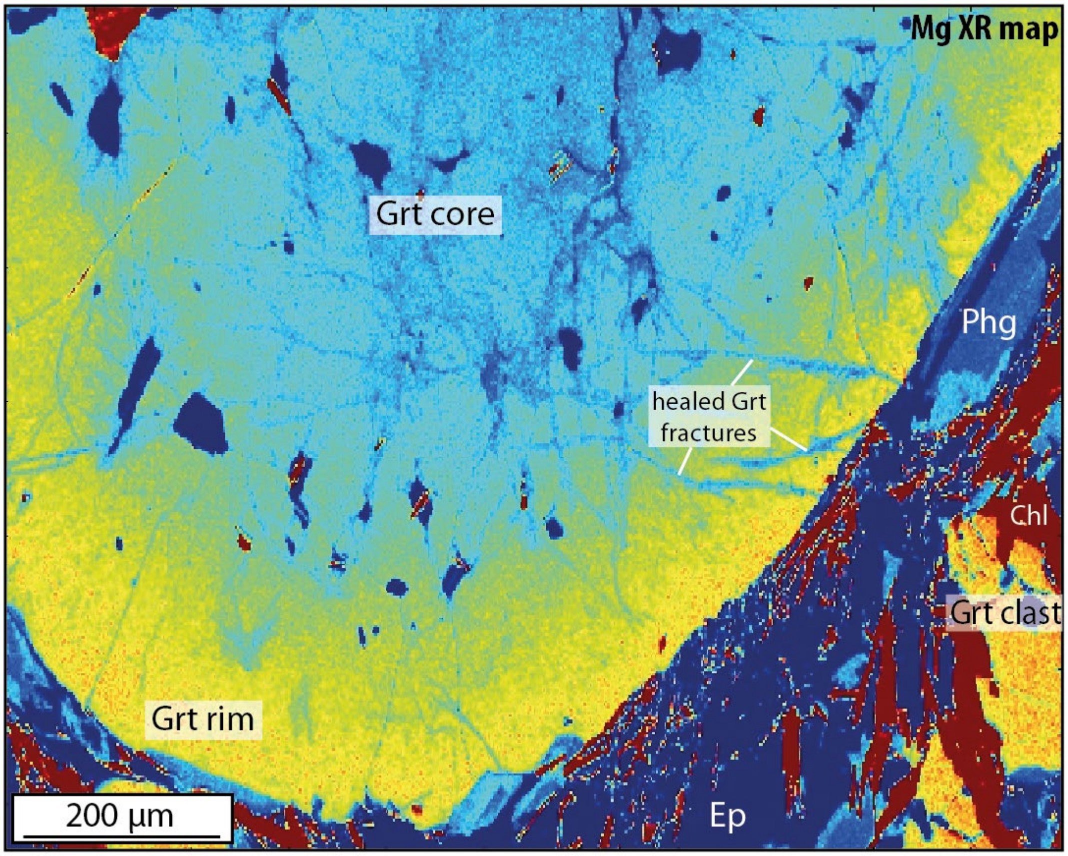


**Figure A.2**: X-ray map (Mg content in counts, warmer colors point to greater concentration) for a garnet from sample #32b and its surrounding matrix. Sample #32b is another metasedimentary sample from the garnet amphibolite unit collected one kilometer north of sample #47a. The image shows a fragmented garnet clast on the right side of the map (surrounded by exhumation-related chlorite flakes) as well as numerous internal healed garnet fractures inside the main garnet crystal. This additional sample indicates that the fracturing event well-visible in #47a is likely a ubiquitous process in all Puerto Shear Zone metasediments.

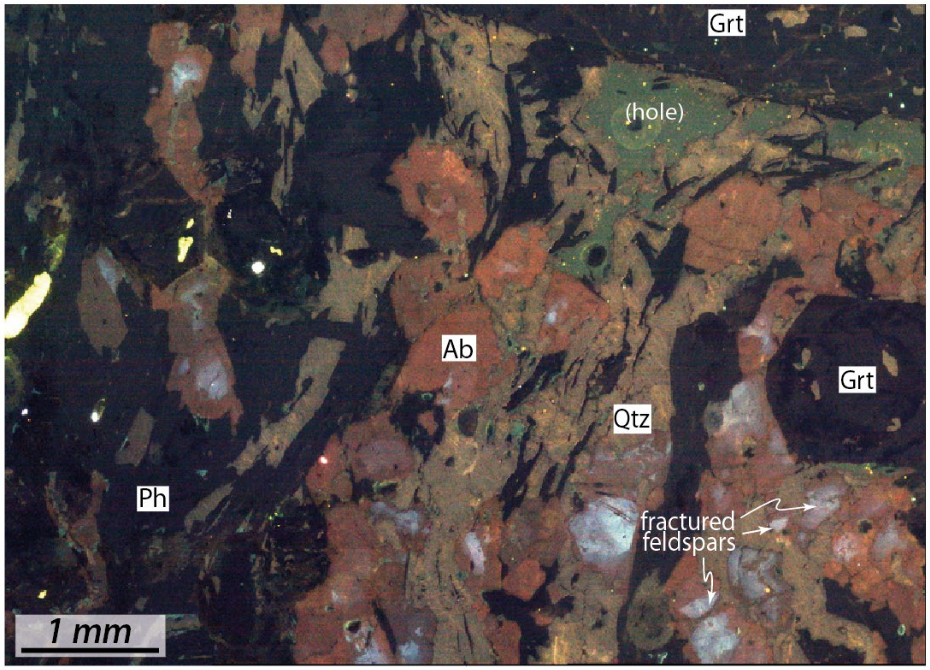


**Figure A.3**: Optical cathodoluminescence picture showing the structure of the matrix in the vicinity of a large garnet crystal. Note the feldspar cores (light grey, slightly Ca-richer) that have been thoroughly fractured, recrystallized and overgrown by an orange-shaded new pure albite generation. Picture taken with a beam of 10 kV, 120 µA and a 2.5 s exposition time (CATHODYNE instrument, NEWTEC company).

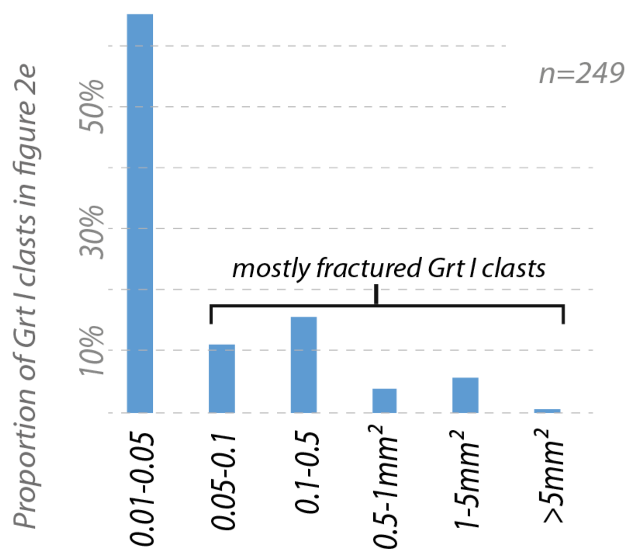


**Figure A.4**: Histogram showing the proportion of the different garnet clast fractions based on the statistical processing of the mosaic image shown in figure 2e.

### Supplementary numerical modelling material:

**Table A.1:** Values of normalized stress, $\sigma_{norm}$, for models with relatively low pore fluid pressure ratios (0.37≤$\lambda$≤0.95). Color-coding corresponds to the style of deformation (dark blue for Style 1; light blue for Style 2; yellow for Style 3, red for Style 4). The bold numbers refer to the lowest and largest $\sigma_{norm}$ values for each deformation style.

| | | Pore fluid ratio | | | | | | | | | | | |
|---|---|---|---|---|---|---|---|---|---|---|---|---|---|
| | | **0.37** | **0.45** | **0.50** | **0.55** | **0.60** | **0.65** | **0.70** | **0.75** | **0.80** | **0.85** | **0.90** | **0.95** |
| Strain rate, log(1/s) | **-6.0** | 1.00 | 1.00 | 1.00 | 1.00 | 1.00 | 1.00 | 1.00 | 1.00 | 1.00 | 1.00 | 1.00 | 1.00 |
| | **-6.5** | 1.00 | 1.00 | 1.00 | 1.00 | 1.00 | 1.00 | 1.00 | 1.00 | 1.00 | 1.00 | 1.00 | 1.00 |
| | **-7.0** | 1.00 | 1.00 | 1.00 | 1.00 | 1.00 | 1.00 | 1.00 | 1.00 | 1.00 | 1.00 | 1.00 | 1.00 |
| | **-7.5** | 0.87 | **0.97** | 1.00 | 1.00 | 1.00 | 1.00 | 1.00 | 1.00 | 1.00 | 1.00 | 1.00 | 1.00 |
| | **-8.0** | 0.68 | 0.76 | 0.81 | 0.88 | 0.96 | 1.00 | 1.00 | 1.00 | 1.00 | 1.00 | 1.00 | 1.00 |
| | **-8.5** | 0.51 | 0.58 | 0.63 | 0.68 | 0.75 | 0.83 | 0.92 | 1.00 | 1.00 | 1.00 | 1.00 | 1.00 |
| | **-9.0** | 0.38 | 0.43 | 0.47 | 0.52 | 0.57 | 0.64 | 0.72 | 0.82 | 0.95 | 1.00 | 1.00 | 1.00 |
| | **-9.5** | 0.29 | 0.32 | 0.35 | 0.39 | 0.43 | 0.48 | 0.55 | 0.63 | 0.74 | 0.89 | 1.00 | 1.00 |
| | **-10.0** | 0.22 | 0.24 | 0.27 | 0.29 | 0.32 | 0.36 | 0.41 | 0.48 | **0.57** | 0.69 | 0.88 | 1.00 |
| | **-10.5** | 0.16 | 0.18 | **0.20** | 0.22 | 0.24 | 0.27 | 0.31 | 0.35 | 0.42 | **0.52** | 0.67 | 0.92 |
| | **-11.0** | 0.12 | 0.14 | 0.15 | 0.16 | 0.18 | **0.20** | 0.23 | 0.27 | 0.32 | 0.39 | 0.51 | 0.71 |
| | **-11.5** | 0.09 | 0.10 | 0.11 | 0.12 | 0.14 | 0.15 | 0.17 | **0.20** | 0.24 | 0.29 | 0.38 | 0.54 |
| | **-12.0** | **0.07** | 0.08 | 0.08 | 0.09 | 0.10 | 0.11 | 0.13 | 0.15 | 0.18 | 0.22 | 0.29 | 0.41 |

**Table A.2:** Values of normalized stress, $\sigma_{norm}$, for models with high pore fluid pressure ratios (0.95≤$\lambda$≤0.995). Color-coding corresponds to the style of deformation (dark blue for Style 1; light blue for Style 2; yellow for Style 3, red for Style 4). The bold numbers refer to the lowest and largest $\sigma_{norm}$ values for each deformation style.

| | | Pore fluid ratio | | | | | | | | | |
|---|---|---|---|---|---|---|---|---|---|---|---|
| | | **0.950** | **0.955** | **0.960** | **0.965** | **0.970** | **0.975** | **0.980** | **0.985** | **0.990** | **0.995** |
| Strain rate, log(1/s) | **-9.0** | 1.00 | 1.00 | 1.00 | 1.00 | 1.00 | 1.00 | 1.00 | 1.00 | 1.00 | 1.00 |
| | **-9.5** | 1.00 | 1.00 | 1.00 | 1.00 | 1.00 | 1.00 | 1.00 | 1.00 | 1.00 | 1.00 |
| | **-10.0** | 1.00 | 1.00 | 1.00 | 1.00 | 1.00 | 1.00 | 1.00 | 1.00 | 1.00 | 1.00 |
| | **-10.5** | 0.92 | 0.96 | 1.00 | 1.00 | 1.00 | 1.00 | 1.00 | 1.00 | 1.00 | 1.00 |
| | **-11.0** | 0.71 | 0.74 | 0.78 | 0.82 | 0.86 | 0.88 | 0.95 | **0.98** | 1.00 | 1.00 |
| | **-11.5** | 0.54 | 0.56 | 0.59 | 0.62 | 0.65 | 0.68 | 0.73 | 0.77 | 0.80 | 0.85 |
| | **-12.0** | 0.41 | 0.42 | 0.45 | 0.47 | **0.49** | 0.52 | 0.55 | 0.58 | 0.62 | 0.66 |
| | **-12.5** | 0.30 | 0.32 | 0.33 | 0.35 | 0.37 | 0.38 | 0.41 | 0.43 | 0.46 | **0.49** |
| | **-13.0** | 0.22 | 0.23 | 0.25 | 0.26 | 0.27 | 0.28 | 0.30 | 0.32 | 0.34 | 0.36 |
| | **-13.5** | 0.17 | 0.18 | 0.19 | 0.20 | 0.21 | 0.22 | 0.23 | 0.25 | 0.26 | 0.28 |
| | **-14.0** | **0.13** | **0.14** | **0.14** | **0.15** | 0.16 | 0.17 | 0.18 | 0.19 | 0.20 | 0.21 |
| | **-14.5** | 0.09 | 0.10 | 0.10 | 0.11 | 0.11 | 0.12 | **0.13** | **0.13** | **0.14** | **0.15** |
| | **-15.0** | **0.08** | 0.08 | 0.09 | 0.09 | 0.10 | 0.10 | 0.11 | 0.11 | 0.12 | 0.13 |